Yield precursor dislocation avalanches in small crystals: the irreversibility transition

Xiaoyue Ni[1,*], Haolu Zhang[1], Danilo B. Liarte[2], Louis W. McFaul[3], Karin A. Dahmen[3], James P. Sethna[2], and Julia R. Greer[1]

[1]*Division of Engineering and Applied Sciences, California Institute of Technology, Pasadena, CA 91125*
[2]*Laboratory of Atomic and Solid State Physics, Cornell University, Ithaca, New York 14853-2501*
[3]*Physics Department, University of Illinois at Urbana-Champaign, Urbana, IL 61810*

The transition from elastic to plastic deformation in crystalline metals shares history dependence and scale-invariant avalanche signature[1–5] with other non-equilibrium systems under external loading: dilute colloidal suspensions[6,7], plastically-deformed amorphous solids[8–11], granular materials[12–15], and dislocation-based simulations of crystals[16]. These other systems exhibit transitions with clear analogies to work hardening and yield stress[17], with many typically undergoing purely elastic behavior only after "training" through repeated cyclic loading; studies in these other systems show a power law scaling of the hysteresis loop extent and of the training time as the peak load approaches a so-called reversible-irreversible transition (RIT)[6,7]. We discover here that deformation of small crystals shares these key characteristics: yielding and hysteresis in uniaxial compression experiments of single-crystalline Cu nano- and micro-pillars decay under repeated cyclic loading. The amplitude and decay time of the yield precursor avalanches diverge as the peak stress approaches failure stress for each pillar, with a power law scaling virtually equivalent to RITs in other nonequilibrium systems.

The mechanical deformation of macroscopic metals is usually characterized by the *yield stress*, below which the metal responds elastically, and beyond which plastic deformation is mediated by complex dislocation motion and interactions. In small-scale crystals, dislocation activities are manifested as avalanches, with characteristic discrete strain bursts in the stress-strain response of the sample[2,18,19]. The yield stress depends on the history of the sample: if the sample were unloaded and then re-loaded during plastic flow, the current yield stress would become the previous maximum stress, below which there are no deviations from linear-elastic response, with the flow and yield stresses always increasing, *i.e. work hardening*[20]. We begin by showing that the 'textbook description' of yield stress and work hardening do not hold for metallic single-crystalline micro- and nano-pillars

* xni@northwestern.edu

under uniaxial loading[†]. Fig. 1(a) shows typical stress-strain responses of displacement-controlled (DC) compression of single-crystalline <111>-oriented copper nanopillars with diameters of 300 nm, 500 nm, 700 nm, 1 μm, and 3 μm. This plot reveals multiple discrete strain bursts, which have been shown to correspond to dislocation avalanches that emanate from their pinning points or sources during plastic flow[21]. Some occasional strain bursts are also present during the post-avalanche reloading processes at stresses lower than the current 'yield stress', which is defined as the previous maximum stress that triggered the most-recent avalanche unloading event, exemplified in Fig 1(b) for the 300 nm diameter pillar test. The presence of such pre-yield avalanches contrasts with the conventional definition of history-dependent yield point in metals that strictly separates the purely elastic behavior upon unloading and reloading from irreversible plasticity. The plastic strain that occurs below the previous maximum stress is the *yield-precursor* strain.

In the experiments presented here, we observed that the larger pillars that were monotonically loaded under displacement control generally produced shorter avalanche strains[22,23] and was less frequently spontaneously unloaded by the instrument compared with the smaller pillars. We conducted load-controlled (LC) compression experiments with several prescribed unload-reload cycles along the quasi-static compression to investigate the effect of system size on precursor avalanche behavior, where "system size" refers to the overall pillar volume. Fig. 1(c) shows such unload-reload stress-strain response of representative 500 nm and 3.0 μm diameter copper pillars, and Fig 1(d) compares their yield-precursor stress-strain response, σ_r *vs.* ε_0, where σ_r is the stress reconstructed as an average of all reloading stresses at a fixed reloading plastic strain ε_0, zeroed at the previous maximum stress (see SI for details of the stress-strain reconstruction procedure). The types of precursor avalanches that we observe during the deformation of micropillars that extend over $\sim 10^{-4}$ strains at precursor stresses that are ~ 60 MPa lower than the previous maximum stress would pose significant corrections to Hookean elastic behavior if they persisted to macroscopic systems.

[†] The textbook picture, of elastic behavior under reloading until the previous stress maximum, has been violated before in polycrystalline metals[30] and small system sizes with unconventional microstructures[31–35] or strong strain gradients[36].

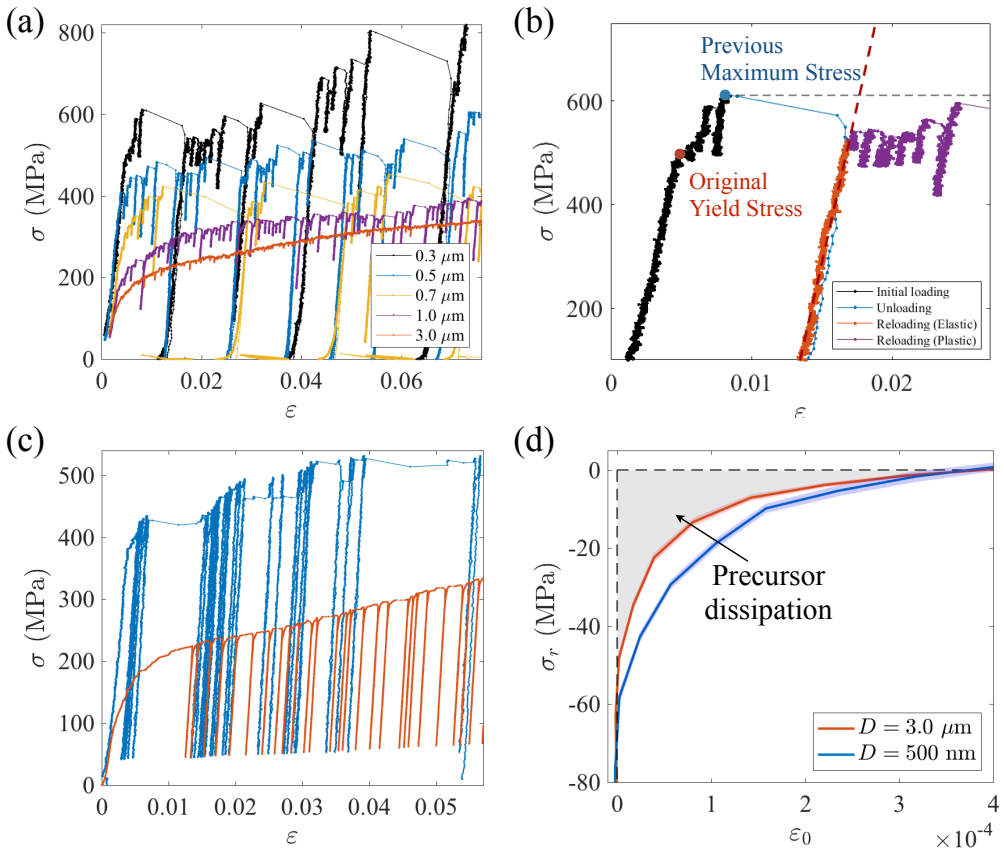

FIG. 1. **Precursor avalanches present in the quasistatic uniaxial and unload-reload cyclic compression experiments on single crystalline copper pillars.** (a) Representative stress-strain data for a displacement-controlled (DC) compression experiment on a 300 nm, 500 nm, 700 nm, 1 μm, and 3 μm diameter pillars. (b) A close-up of a fast-avalanche induced unloading-reloading process in the 300 nm diameter pillar compression test. The data starts to deviate from linear elastic response at a strain of ~ 0.017, while at a stress lower than the updated 'yield stress', defined as the previous maximum stress. (c) Sample stress-strain and (d) the reconstructed non-Hookean stress-strain for two representative load-controlled (LC) unload-reload compression experiments (see SI for detailed reconstruction procedures) on 3 μm and 500 nm diameter pillars. The area of the shaded region represents precursor dissipation for 3 μm pillars.

We numerically evaluated the energy per volume dissipated by the precursor avalanches in each cycle, the *precursor dissipation*, from an integral over the reconstructed stress-strain hysteresis, $U = \int \sigma_r d\varepsilon_0$, indicated by the shaded area in Fig. 1 (d) for 3 μm diameter samples. We observed larger precursor dissipation in smaller pillars, which suggests that the precursor avalanches may disappear in macroscopic samples, perhaps explaining why it has not been thoroughly examined in existing literature.

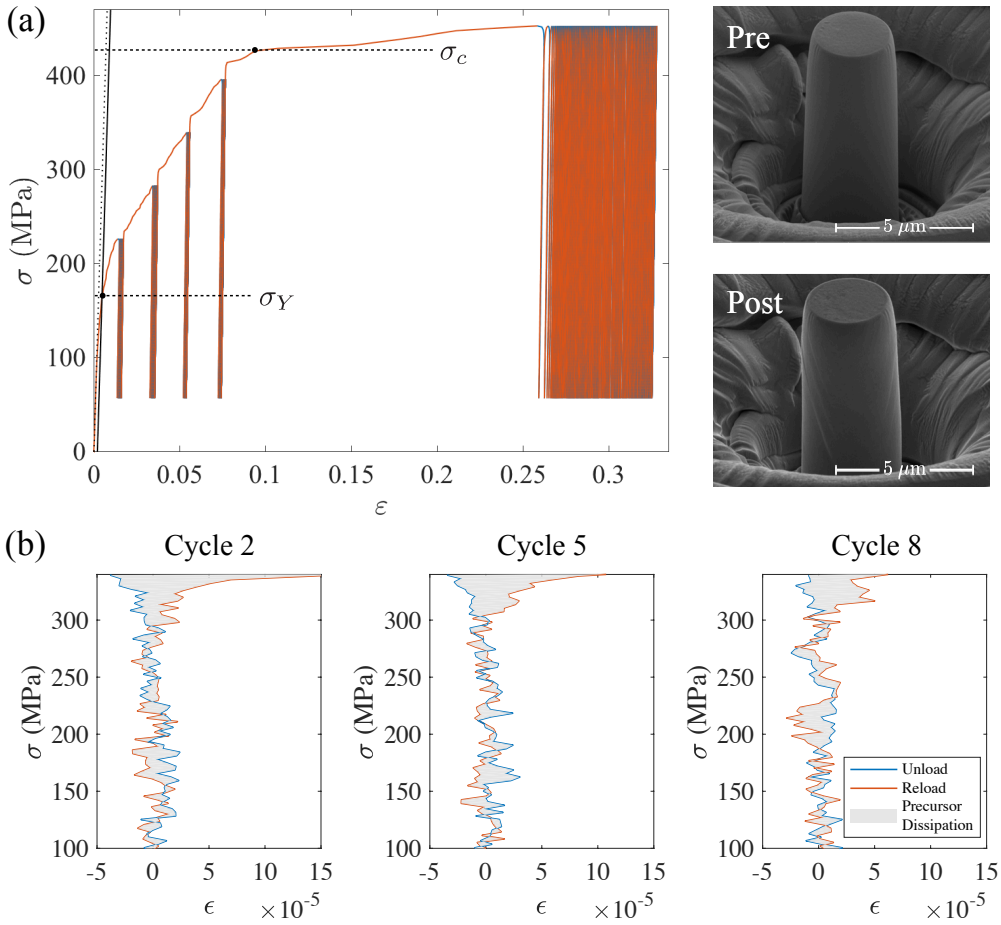

FIG. 2. **Precursor avalanches trained over cyclic loading in micro-pillars**. (a) Left: stress-strain response from a training experiment on a 3 μm-diameter copper pillar. Unloading and reloading stress-strain curves are marked in blue and red, respectively. Yield stress σ_Y is defined as the intersection between the stress-strain data and the 0.2% strain offset elastic loading segment. The maximum stress is increased in five steps; step 5 is above the failure stress σ_c. At each step, 100 unload-reload cycles are prescribed. Right: pre- and post-test scanning electron microscope (SEM) images of this sample that show crystallographic slip lines on parallel planes characteristic of dislocation avalanches and glide. (b) The drift-corrected stress vs. strain (See SI for details) during the 2nd, 5th, and 8th cycles from data shown in (a) loaded to a maximum of ~ 340 MPa. Shaded area represents the energy dissipated through precursor avalanches, which decreases over cyclic loading.

We conduct cyclic loading experiments to study how the precursor hysteresis changes under repeated loading to the same maximum stress, analogous to experiments on other non-equilibrium systems[6,7]. We choose 3 μm diameter single crystalline copper pillars as the primary experimental system because it is sufficiently large amongst the "small-scale" counterparts to exhibit failure under quasistatic loading as well as relatively deterministic precursor avalanche behavior. Figure 2 (a) shows the stress-strain data from three representative experiments on the left along with the scanning electron microscope (SEM) images of a typical pillar pre- and post-compression on the right. We define the yield stress

σ_Y according to the standard engineering criteria as the intersection between the stress-strain data and the 0.2% strain offset elastic loading segment, which gives ~160 MPa for the $3\ \mu m$ diameter copper pillars. The failure stress, σ_c, defined as the stress beyond which the samples are no longer able to support additional applied load, is ~ 420 MPa. Above this stress, the sample continually deforms plastically at a constant stress. We prescribe five maximum cyclic stress steps from 228 MPa (0.54 σ_c) to 452 MPa (1.08 σ_c) at equal stress intervals of 56 MPa (0.13 σ_c). In each stress step, we apply 100 unload-reload cycles, during which the sample is loaded to the same maximum stress and unloaded to a minimum of 56 MPa to maintain contact between the compression tip and the sample. We investigate the yield precursor dissipation evolution over all cycles at each stress step. Figure 2 (b) shows the 2nd, 5th and 8th cycles of drift-corrected data (See SI for details) cycled to 340 MPa shown in Fig. 2 (a), with precursor dissipation indicated by the shaded areas.

We apply the same multistep cyclic load function to nine identically prepared samples. It is reasonable to assume that for a cycle at a specific stress step, the intrinsic precursor dissipation behavior is equivalent across all samples within statistical variation. Figure 3 (a) shows the average and standard error of the precursor dissipation as a function of cycle number for increasing stress steps. These plots unambiguously demonstrate the *training* phenomenon: the precursor hysteresis decays with cycling. Increasing the maximum stress triggers new precursor avalanches and new training cycles. Below the catastrophic failure stress σ_c, the precursor dissipation virtually vanishes. Above the failure stress, the hysteretic dissipation continues beyond the prescribed 100 stress cycles, which indicates that the training is incomplete.

We characterize the decay of precursor dissipation, U, versus number of cycles, n, using a fitting function $U_f(n)$[7],

$$U_f(n) = (U_0 - U_\infty)e^{-n/\tau}n^{-\delta} + U_\infty,$$

where $U_\infty = U_f(n \to \infty)$ is the estimated steady-state dissipation (See SI for details). U_0 is the initial dissipation. The power law decay of U_f hints at the fluctuation behavior near the critical point. This analysis reveals that the catastrophic failure stress σ_c in these experiments can be associated with the reversible-to-irreversible transition (RIT) critical stress. This association is corroborated by the non-zero limiting dissipation U_∞ for a maximum stress amplitude of $\sigma_{max} > \sigma_c$. We approximate the long-term decay at the last step at $\sigma_{\max} = 1.08\ \sigma_c$ as critical behavior and fit the precursor dissipation $U(n)$ using the simple power law function, $U_f'(n) = U_f(n;\ \tau \to \infty, U_\infty \to 0) = U_0 n^{-\delta}$, to estimate the exponent δ. We apply the fitted power-law exponent $\delta = 0.68 \pm 0.02$ to determine τ for the remaining stress steps.

Figure 3 (b) shows that the decay time constant of precursor avalanches τ increases with maximum stress $\sigma_{\max}$. Plotting the characteristic time scale, τ, as a function of proximity to critical point on a log-log scale in Figure 3 (c), we find a striking resemblance to the colloidal suspension systems, which indicates that stress-driven dislocations in small-scale metals exhibit RIT behavior similar to that seen in sheared colloidal particles[7].

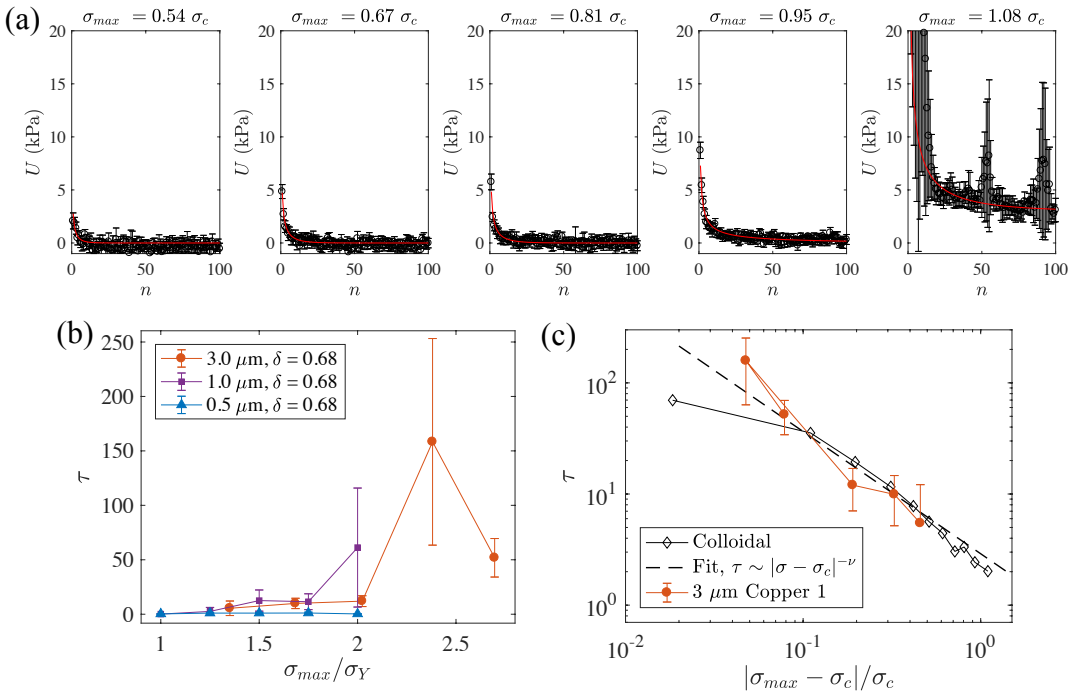

FIG. 3. **Training experimental results showing precursor dissipation activity at different maximum stresses**. (a) The precursor dissipation energy U decays with the number n of prior loading cycles at each maximum stress. The number of cycles necessary to reach steady state increases with increasing maximum stress $\sigma_{\max}$. (b) The characteristic decay time τ versus maximum stress $\sigma_{\max}$ estimated for different pillar sizes (See SI for details). For large pillars, the number of cycles necessary to reach the reversible state increases with applied maximum stress. (c) A direct comparison of dislocation RIT behavior gleaned from the copper micropillar compression experiments with that reported for a colloidal particle system in sheared suspension[7], which provides evidence for a divergence of necessary cycle time τ to reach a reversible state, close to the critical failure stress σ_c.

Analogous to the colloidal suspension systems, it is plausible that at low stresses, the strongly interacting dislocations in the pillars may rearrange themselves into a stable configuration as the system reloads the first time. At higher peak stresses, the dislocation rearrangements in one cycle may trigger a cascade of further avalanches in subsequent cycles. In small-scale crystalline plasticity, the RIT corresponds to the stress at which additional cycling continues to plastically deform the system with no additional applied forces, which corresponds to the failure stress.

We can speculate about the relation between the critical behavior of the precursor avalanches observed here and the power-law distribution of dislocation avalanches observed in nano- and micropillars under monotonic loading. The precursor avalanches at an RIT usually diverge in size only near the failure stress. Plasticity avalanches under monotonic loading are usually considered to be a 'self-organized criticality', which exhibits a power law scaling along the entire loading curve[1–5]. Friedman et al.[24] measured a cutoff in the avalanche size distribution that diverged only as the stress approaches the 'failure' stress'[25] – precisely as one would expect for the approach to an RIT.

In this work, we bring attention to the overlooked signature of yield precursor avalanches in nanomechanical experiments. We show that the amount of dissipation due to yield precursor avalanches decays over repeated stress training cycles. This training behavior is reminiscent of prior research on ratcheting in fatigue deformation [26,27], as well as the unloading effect on the yield point phenomena[28,29]. We find that the characteristic decay time increases with the applied maximum stress. The apparent divergence of the time constant at a maximum stress near the quasistatic failure stress indicates that the flow transition of the dislocation system is fundamentally a reversible-to-irreversible transition. These observations may lead to a better understanding of plasticity and catastrophic failure in crystalline materials governed by complex dislocation dynamics. This fundamental connection between dislocation systems and other non-equilibrium systems can provide new insights into microstructural design of novel materials.

ACKNOWLEDGEMENT:

J.R.G. and X.N. acknowledges financial support from the U.S. Department of Energy's Office of Basic Energy Sciences through grant DESC0016945. J.P.S. and D.L. acknowledge the financial support of the U.S. Department of Energy's Office of Basic Energy Sciences through Grant DE-SC0006599 and NSF grant DMR-1719490. K.A.D acknowledges NSF grant CBET 1336634. We thank Stefano Zapperi and Giulio Costantini, D. Zeb Rocklin, Archishman Raju, and Lorien Hayden for helpful discussions.

REFERENCES:

1. Miguel, M. C., Vespignani, A., Zapperi, S., Weiss, J. & Grasso, J. R. Intermittent dislocation flow in viscoplastic deformation. *Nature* **410,** 667–71 (2001).
2. Dimiduk, D. M. Scale-Free Intermittent Flow in Crystal Plasticity. *Science* **312,** 1188–1190 (2006).
3. Weiss, J. *et al.* Evidence for universal intermittent crystal plasticity from acoustic emission and high-resolution extensometry experiments. *Phys. Rev. B - Condens. Matter Mater. Phys.* **76,** 1–8 (2007).
4. Ng, K. S. & Ngan, A. H. W. Creep of micron-sized aluminium columns. *Philos. Mag. Lett.* **87,** 967–977 (2007).
5. Zaiser, M. *et al.* Strain bursts in plastically deforming molybdenum micro- and nanopillars. *Philos. Mag.* **88,** 3861–3874 (2008).
6. Pine, D. J., Gollub, J. P., Brady, J. F. & Leshansky, A. M. Chaos and threshold for irreversibility in sheared suspensions. *Nature* **438,** 997–1000 (2005).
7. Corté, L., Chaikin, P. M., Gollub, J. P. & Pine, D. J. Random organization in periodically driven systems. *Nat. Phys.* **4,** 420–424 (2008).
8. Regev, I., Lookman, T. & Reichhardt, C. Onset of irreversibility and chaos in amorphous solids under periodic shear. *Phys. Rev. E - Stat. Nonlinear, Soft Matter Phys.* **88,** 1–5 (2013).
9. Regev, I., Weber, J., Reichhardt, C., Dahmen, K. A. & Lookman, T. Reversibility and criticality in amorphous solids. *Nat. Commun.* **6,** 8805 (2015).
10. Jeanneret, R. & Bartolo, D. Geometrically protected reversibility in hydrodynamic Loschmidt-echo experiments. *Nat. Commun.* **5,** 3474 (2014).
11. Hima Nagamanasa, K., Gokhale, S., Sood, A. K. & Ganapathy, R. Experimental signatures of a nonequilibrium phase transition governing the yielding of a soft glass. *Phys. Rev. E - Stat. Nonlinear, Soft Matter Phys.* **89,** 1–7 (2014).
12. Rogers, M. C. *et al.* Echoes in x-ray speckles track nanometer-scale plastic events in colloidal gels under shear. *Phys. Rev. E - Stat. Nonlinear, Soft Matter Phys.* **90,** 1–7 (2014).
13. Möbius, R. & Heussinger, C. (Ir)reversibility in dense granular systems driven by oscillating forces. *Soft Matter* **10,** 4806–12 (2014).
14. Schreck, C. F., Hoy, R. S., Shattuck, M. D. & O'Hern, C. S. Particle-scale reversibility in athermal particulate media below jamming. *Phys. Rev. E - Stat. Nonlinear, Soft Matter Phys.* **88,** 1–9 (2013).
15. Slotterback, S. *et al.* Onset of irreversibility in cyclic shear of granular packings. *Phys. Rev. E - Stat. Nonlinear, Soft Matter Phys.* **85,** 1–5 (2012).
16. Zhou, C., Reichhardt, C. J. O., Reichhardt, C. & Beyerlein, I. Random Organization in Periodically Driven Gliding Dislocations. 1–5 (2013).
17. Sethna, J. P. *et al.* Deformation of Crystals: Connections with Statistical Physics. *Annu. Rev. Mater. Res* **47,** 217–46 (2017).
18. Uchic, M. D. Sample Dimensions Influence Strength and Crystal Plasticity. *Science* **305,** 986–989 (2004).
19. Greer, J. R., Oliver, W. C. & Nix, W. D. Size dependence of mechanical properties of gold at the micron scale in the absence of strain gradients. *Acta Mater.* **53,** 1821–1830 (2005).

20. Lubliner, J. *Plasticity Theory*. (Macmillan, 1990).
21. Zaiser, M. Scale invariance in plastic flow of crystalline solids. *Adv. Phys.* **55,** 185–245 (2006).
22. Csikor, F. F., Motz, C., Weygand, D., Zaiser, M. & Zapperi, S. Dislocation Avalanches, Strain Bursts, and the Problem of Plastic Forming at the Micrometer Scale. *Science.* **318,** 251–254 (2007).
23. Brinckmann, S., Kim, J. Y. & Greer, J. R. Fundamental differences in mechanical behavior between two types of crystals at the nanoscale. *Phys. Rev. Lett.* **100,** 1–4 (2008).
24. Friedman, N. *et al.* Statistics of dislocation slip avalanches in nanosized single crystals show tuned critical behavior predicted by a simple mean field model. *Phys. Rev. Lett.* **109,** 1–5 (2012).
25. Dahmen, K. A., Ben-Zion, Y. & Uhl, J. T. Micromechanical model for deformation in solids with universal predictions for stress-strain curves and slip avalanches. *Phys. Rev. Lett.* **102,** 1–4 (2009).
26. McDowell, D. L. Stress state dependence of cyclic ratchetting behavior of two rail steels. *Int. J. Plast.* **11,** 397–421 (1995).
27. Radhakrishnan, V. M. Stress ratchetting under tension and cyclic torsion. *Nucl. Eng. Des.* **34,** 379–387 (1975).
28. Haasen, P. & Kelly, A. A yield phenomenon in face-centered cubic single crystals. *Acta Metall.* **5,** 192–199 (1957).
29. Brown, L. M. An interpretation of the Haasen–Kelly effect. *Philos. Mag.* **90,** 4147–4152 (2010).
30. Cleveland, R. M. & Ghosh, A. K. Inelastic effects on springback in metals. *Int. J. Plast.* **18,** 769–785 (2002).
31. Xiang, Y. & Vlassak, J. J. Bauschinger and size effects in thin-film plasticity. *Acta Mater.* **54,** 5449–5460 (2006).
32. Jennings, A. T. *et al.* Higher compressive strengths and the Bauschinger effect in conformally passivated copper nanopillars. *Acta Mater.* **60,** 3444–3455 (2012).
33. Rajagopalan, J., Han, J. H. & Saif, M. T. A. Plastic Deformation Recovery in Freestanding Nanocrystalline Aluminum and Gold Thin Films. *Science* **315,** 1831 LP-1834 (2007).
34. Brown, J. A. & Ghoniem, N. M. Reversible-irreversible plasticity transition in twinned copper nanopillars. *Acta Mater.* **58,** 886–894 (2010).
35. Bernal, R. A. *et al.* Intrinsic bauschinger effect and recoverable plasticity in pentatwinned silver nanowires tested in tension. *Nano Lett.* **15,** 139–146 (2015).
36. Liu, D. *et al.* Anomalous plasticity in the cyclic torsion of micron scale metallic wires. *Phys. Rev. Lett.* **110,** 1–5 (2013).

Appendix A: Experimental method

We use single-crystalline FCC copper micropillars as our study system. We fabricate the cylindrical samples from a bulk single-crystalline copper (purchased from MTI Corporation) that is of purity > 99.9999% and with top surface polished to $a < 30$Å RMS roughness, following a concentric-circles top-down methodology using a Focused Ion Beam. We use 30 kV gallium ion beam starting with an ion current of 5 nA for outer rings milling, and reduce the current in steps to 30 pA for the finish up in order to suppress gallium ion implantation as well as sidewall tapering. The pillar diameters range from 0.3 to 3 μm with aspect ratios (height/diameter) of ~ 3:1. The mechanical properties of the exact 0.5 μm pillar arrays tested have been reported in Ref. [1]. The sample is oriented in the ~ <111> loading direction. We carry the nanomechanical experiments in a nanoindenter (Triboindenter, Hysitron) equipped with a custom made 8 μm-diameter diamond flat punch. Both load controlled and displacement controlled loading modes were used.

Appendix B: Reconstruction of reloading stress-strain

In this paper, we apply a reloading stress-strain reconstruction protocol to analyze the yield-precursor behavior for different sizes of pillars. Fig S1 (a) shows a sample stress-strain data of load-controlled (LC) uniaxial compression tests on 500 nm diameter pillars with prescribed unload-reload cycles. The cyclic loading rate is ~ 400 MPa, while the maximum stress is ramped up at a rate of ~ 5 MPa/cycle, which is equivalent to a quasistatic ramping rate of ~ 1.4 MPa/s. We keep the minimum stress at ~ 40 MPa to maintain tip-sample contact. As the occurrence of avalanches upon reloading is stochastic in small-scale crystals, the main purpose of the stress-strain reconstruction is to average all the reloading curves as a measure of the ensemble precursor deviation from the textbook 'peak stress' yield point.

We first shift the origin of each reloading process such that the stress is zeroed at the previous maximum stress (start of unloading) and the strain is zeroed at the beginning of each reloading, which is shown in Fig. S1 (b). During reloading, if a new avalanche happens before reaching the previous maximum stress (re-zeroing stress), it is a precursor avalanche.

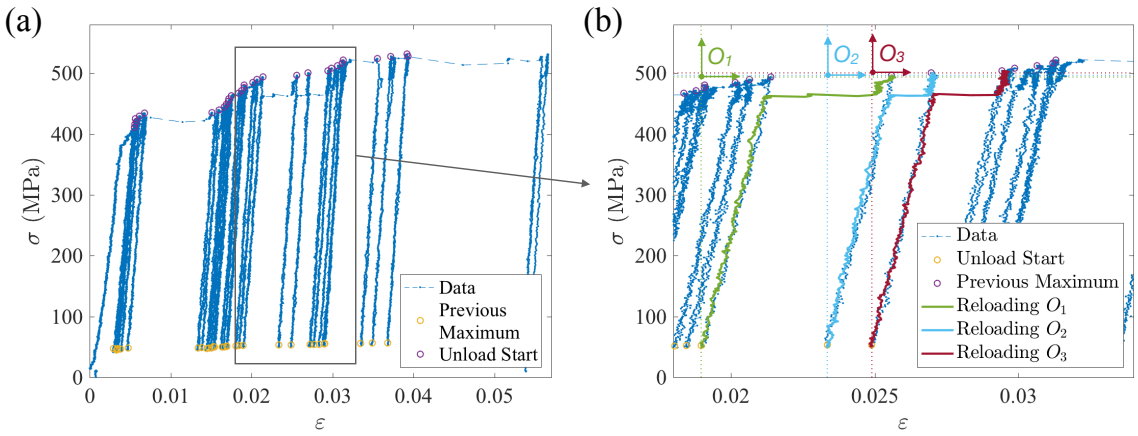

FIG. S1. **Re-zeroing reloading stress-strain in unload-reload experiments:** (a) A sample stress-strain curve for unload-reload tests on a 0.5 μm copper pillar, marked with the onset and finish of each avalanche event and (b) a closer look at the sample unload-reload cycles, where the stress after each unloading is re-zeroed with the previous maximum stress (textbook new yield stress) and the strain is re-zeroed with the starting strain of the reloading process. The shifted stress-strain origin is labeled as O_1 for the first marked reloading process, O_2 for the second, and so on.

Each re-zeroed reloading process for any pillar is then treated as an individual reloading test on one nanopillar. The total precursor behavior for the pillars can be reconstructed according to a Gedanken experiment on a macroscopic sample composed of stacks of nanopillars either in parallel or in series, as illustrated in Fig. S2 (a). We interpolate and average the reloading response of each pillar along the monotonically increasing strain ε_0 (in-parallel) or stress σ_0 (in-series) for the ensemble response. Fig. S2 (b) shows examples of the in-series and in-parallel interpolation of the single reloading curve shown in Fig. S1(b) and zeroed at O_1.

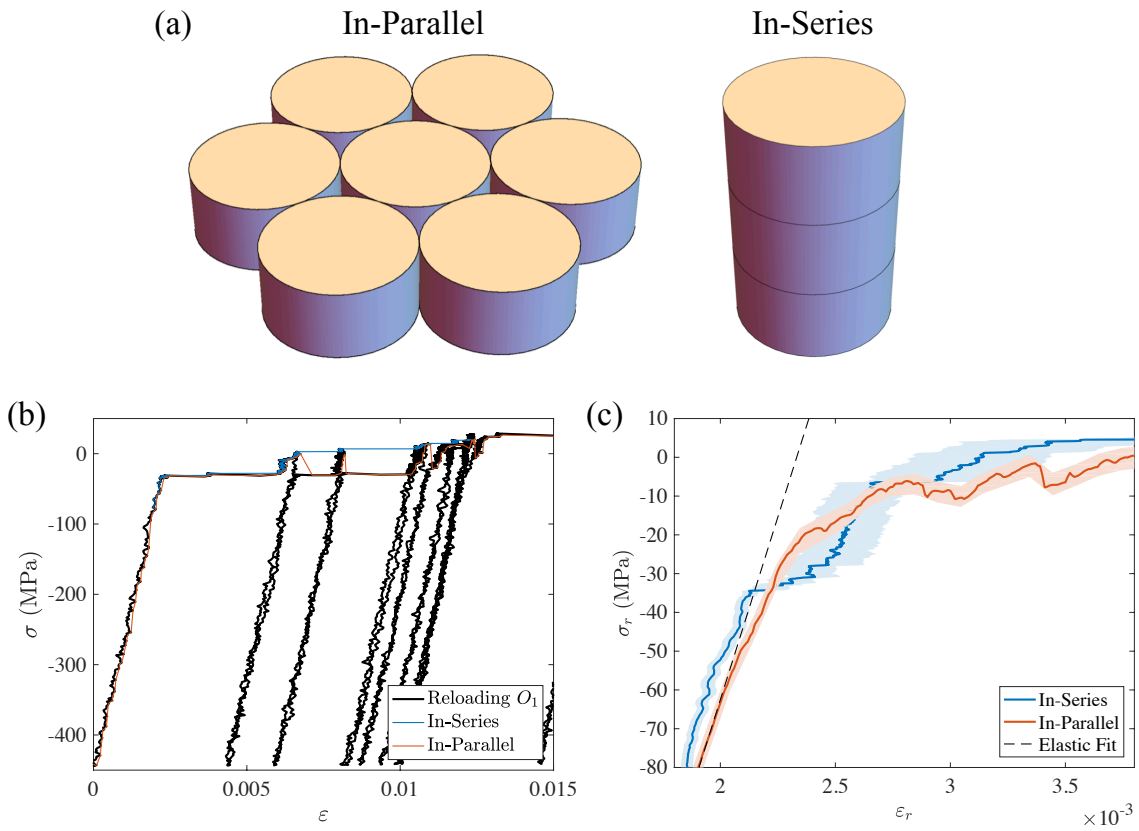

FIG. S2. **Stress-strain reconstruction according to Gedanken compression experiments on micropillars** (a) Schematics of Gedanken compression experiments with prescribed strain (in-parallel) and prescribed stress (in-series) configurations. (b) Examples of in-series strain and in-parallel stress interpolation of the single reloading curve shown in Fig. S1(b) and zeroed at origin 0_1. (c) The averaging stress-strain reconstruction of the reloading curves for both in-parallel and in-series cases for the sample load-controlled test shown in Fig S1.

In the parallel configuration, for the i^{th} pillar, strain $\varepsilon_i = \varepsilon_0$ is controlled and stress σ_i encodes the material's response. The system composed of N pillars has a stress response,

$$\begin{aligned}\sigma_r &= \frac{1}{N}\sum_{i=1}^{N}\sigma_i \\ &= \frac{1}{N}\sum_{i=1}^{N}(E_i + \delta E_i)\varepsilon_0 \\ &= E\varepsilon_0 + \frac{1}{N}\sum_{i=1}^{N}\delta E_i \varepsilon_0 \\ &= (E + \delta E)\varepsilon_0.\end{aligned}$$

In Eq. (1) $\delta E = \frac{1}{N}\sum_{i=1}^{N} \delta E_i$ characterizes the plastic response of the N-pillar system. σ_r and ε_0 are the reconstructed stress and strain. Similarly, the series reconstructed strain ε_r can be expressed with respect to the prescribed stress σ_0,

$$\varepsilon_r = (E + \delta E)^{-1}\varepsilon_0.$$

Fig. S2 (c) shows the sample in-series and in-parallel averaging reconstruction of reloading stress and strain for the same unload-reload test on single 0.5 μm diameter copper pillar as shown in Fig 1. In the main text we present the in-parallel reconstruction for tests on seven 0.5 μm diameter copper pillars. We keep only the Non-Hookean part of strain in the final results by subtracting the elastic strain from the linear fit of stress-strain in the elastic reloading regime, $\sigma_r \in [-300, -100]$ MPa. The elastic fit for the sample in-parallel reconstruction stress-strain is shown in Fig S2 (c).

The same reconstruction analysis can be applied to the conventional load- or displacement-controlled nanomechanical experiments. In the quasi-static, uniaxial loading experiments, the plastic strain bursts usually lead to a drop in the applied force caused by the finite machine stiffness under either displacement or load control. Fig. S3 (a) shows a sample stress-strain of a load-controlled compression test on a 0.5 μm diameter copper pillar, marked with the onset and finish of each avalanche event: at the beginning of a displacement burst of size Δx, the force applied to the sample drops by $k\Delta x$, with k being the machine stiffness. Driven by the feedback control, the indenter tip will re-attain the prescribed load on the sample after a fast avalanche event is completed. This stress-drop-and-catch-up process is manifested as a spontaneous unload-reload response. The stress that initiates an avalanche can be regarded as the updated yield stress of the deformed pillar. The yielding avalanche triggers the following unloading process. When the avalanche finishes, the load/displacement control re-engages and starts the reloading process.

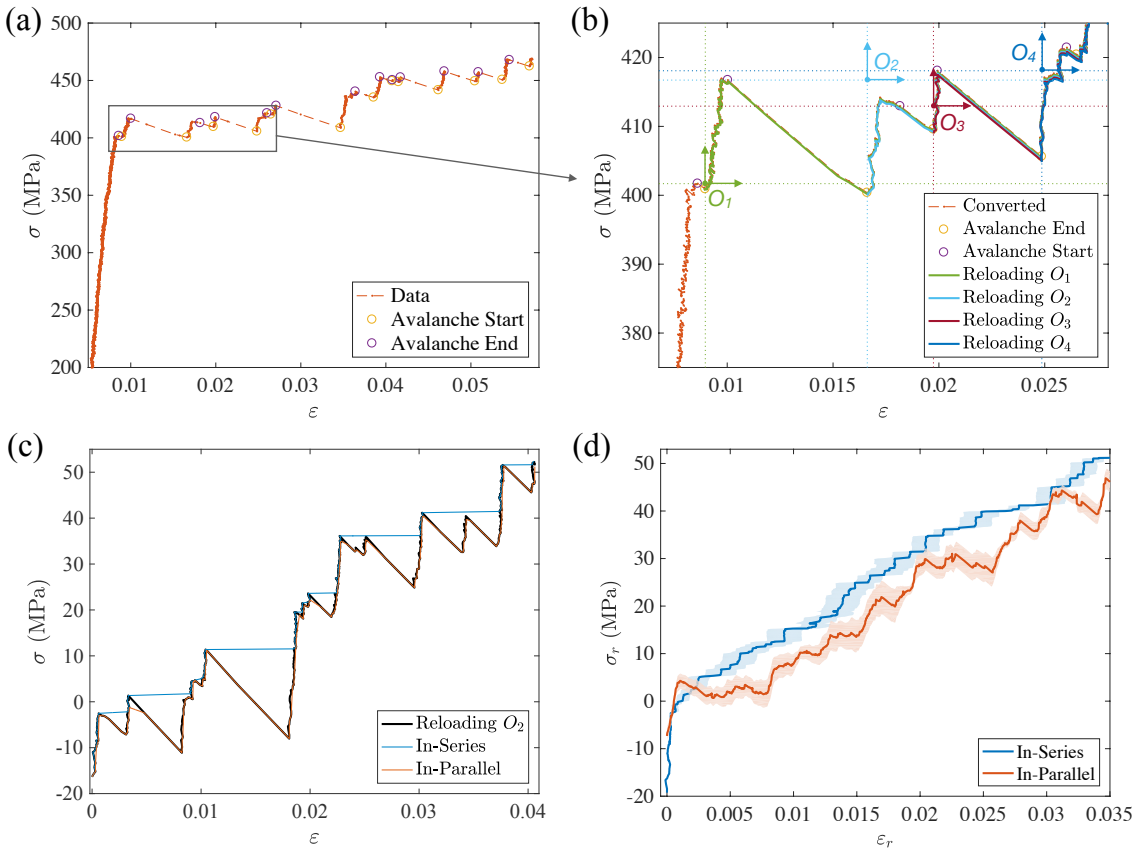

FIG. S3. **Stress-strain reconstruction for finding precursor avalanches in quasistatic load-controlled experiment:** (a) A sample stress-strain curve for load-controlled tests on a 0.5 μm copper pillar, marked with the onset and finish of each avalanche event and (b) a closer look at the avalanches, where the stress after each avalanche is re-zeroed with the previous maximum stress (textbook new yield stress) and the strain is re-zeroed with the starting strain of the reloading process. The re-zeroed stress-strain origin is marked as O_1 for the first seen avalanche, O_2 for the second, and so on. (c) Examples of in-series strain and in-parallel stress interpolation of the single reloading curve shown in (b), zeroed at origin O_1. (d) The averaging stress-strain reconstruction of the reloading curves for both in-parallel and in-series cases for the sample load-controlled test shown in (a).

Fig. S3 (b-d) exemplify the reconstruction process for the load-controlled experiment shown in Fig S3 (a) following the same protocol as the one applied to the unload-reload experiments: (b) we shift origins of the stress-strain data after each yielding avalanche with the stress zeroed at the start of the avalanche and strain zeroed at the end of the avalanche, (c) interpolate the in-series strain or in-parallel stress, and (d) take averages of the interpolated strain/stress for the strain/stress reconstruction.

Appendix C: Precursor avalanches in different loading modes

We performed the stress-strain reconstruction analysis for displacement-controlled and load-controlled quasistatic compression tests, in addition to the unload-reload cyclic compression tests. The sample stress-strain measurements for different size samples are shown in Fig. S4 (a-c), while the reconstructed reloading curves are correspondingly shown in Fig. S4 (d-e). Each reconstruction analysis takes averages of all reloading curves from five to seven individual tests on copper pillars. We have subtracted the elastic strain from the reconstructed strain, leaving only the plastic precursor strains. The reconstructed non-Hookean reloading curves are quantitative evaluations for the averaging yield-precursor dissipation of each sizes of copper pillars.

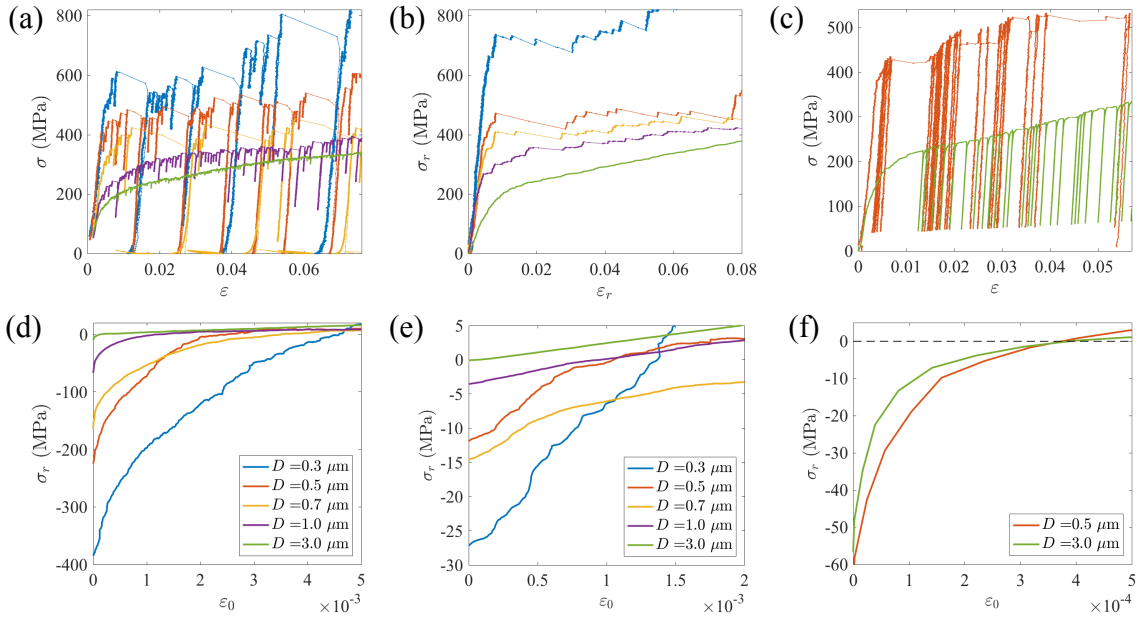

FIG. S4. **Precursor avalanches present in the different loading-mode uniaxial compression experiments on single crystalline copper pillars.** Sample stress-strain (top) and reconstructed non-Hookean stress-strain (bottom) for (a, d) displacement-controlled (DC) monotonic-loading, (b, e) load-controlled (LC) monotonic-loading, and (c, f) unload-reload cyclic-loading compression experiments on different size pillars. In general, less precursor dissipation is observed in larger system.

In all cases, precursor dissipations are prevalently observed in small pillars. We can gain some insights into the precursor avalanches behavior from a comparison amongst the different loading modes results. 1. Larger precursor strains are observed in displacement controlled tests than load-controlled tests. As shown in Fig. S4 (a) and (b), the avalanche-induced unloading amplitudes in displacement controlled tests are on average larger than those in the load controlled experiments. This might infer that the size of precursor strains is dependent on unloading stress amplitude. 2. The precursor strains in unload-reload tests

are much smaller than those of the displacement controlled tests, though the unloading amplitude is of the similar scale. One possible explanation is that part of the "precursor strains" observed in the quasistatic compression tests are "unfinished" avalanches caused by non-perfect control: unlike the prescribed unloading in unload-reload tests, unloading processes in the monotonic loading test are spontaneously triggered by fast avalanches; thus, stress always drops during a slip event, which might interrupt the growing avalanche, leaving residual avalanche to be re-activated upon the subsequent reloading process. 3. Larger precursor dissipations are observed in smaller pillars. This emergent size dependency can be an intrinsic size effect of materials' yield precursor behavior; on the other hand, it can also be a result of smaller pillars undergoing larger unloading amplitude as shown in Figure S4 (a) and (b) – smaller pillars exhibit larger strain bursts, which in turn, will give larger stress drops due to the inherent machine stiffness in both displacement- and load-controlled tests. We have also applied our analysis to simulated data (using 3D discrete dislocation dynamics), and observed similar qualitative behavior (G. Costantini and S. Zapperi, unpublished). Further investigation on the emergent size effect, e.g. doing same-amplitude unload-reload tests on different sizes of pillars, is beyond the scope of this work.

Appendix D: Drift correction in training experiment

In the training experiment, we study how the precursor behavior changes over repeating a hundred unload-reload cycles at the same maximum stress. We evaluate the energy dissipated by precursor avalanches from an integral over each-cycle reconstructed stress-strain hysteresis, $U = \int \sigma d\varepsilon$. During tests with long unloading/reloading segment times, the instrumental drift in the machine can result in large discrepancies between the measured displacements and the actual sample displacements. This can give rise to errors in the calculation of the precursor hysteresis, which is very sensitive to the measurement of displacements during each unloading/reloading cycle. Fig. S5 (a) and (b) demonstrates the drift problem by comparing precursor hysteresis calculated over cycles at the same maximum stress ~ 350 MPa for 3 μm diameter pillars between tests with 2 s (short), 80 MPa amplitude unloading/reloading segments and tests with 4 s (long), 160 MPa amplitude unloading/reloading segments. Both tests use the same loading rate of 40 MPa/s. For the 4 s segments tests shown in Fig. S5 (b), the precursor dissipation decays to negative values, which is unphysical for a uniaxial compression test on single crystalline metals. The unphysical negative hysteresis that is slowly-varying over time can be explained by the usually negative thermal drift present in the nanoindentation tests. We applied drift correction for each unloading/reloading cycle. Fig. S5 (c) shows the post-drift-correction precursor hysteresis vs. cycle data for the same set of tests with 4 s segments, which

mitigates the unphysical negative values and exhibit similar behavior as the short segments test.

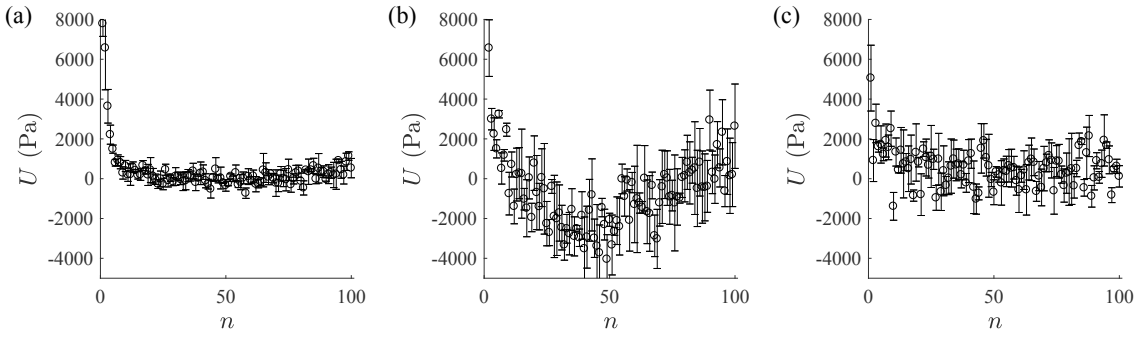

FIG. S5. **Effect of thermal drift on the calculated precursor dissipation for 3μm diameter pillars.** (a) Tests with 2 s (short) individual unloading/reloading segments, which shows a clean decay to zero in the calculated average precursor dissipation. (b) Average precursor dissipation for tests with 4 s (long) unloading/reloading segments, which exhibit unphysical negative values, indicating error in the strain measurements and (c) the same set of tests after drift correction, which gets rid of the negative values and presents a clean decay.

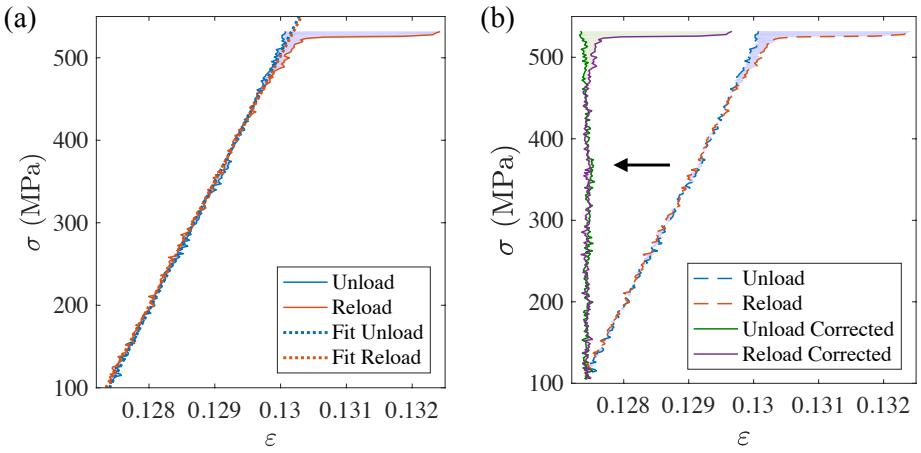

FIG. S6. **Demonstration of the drift correction process**: (a) An example raw stress vs. strain data of subsequent unloading and loading segments; the unloading segment and the loading segment are individually linearly fitted to account for slow instrumental drift in addition to the Hookean elastic strain. The loading segment is fitted using the data excluding the top 80 MPa segment within which precursor avalanches are present. (b) The strains of the linear fits were subtracted from the unloading and loading segments respectively, to correct for the instrumental drift. The filled area in all three plots indicates the precursor area calculated from its corresponding set of data.

The drift correction is done to each unloading/reloading segments as the following. We take one raw stress-strain cycle shown in Fig. S6 (a) as an example. The precursor hysteresis associated to the cycle is marked by the shaded area. Since the individual unloading/reloading segments are short compared to the full test time (usually on the scale

of 400 s), the drift rate during each segment is assumed to be constant. A linear fit is prescribed to each unloading/reloading segment below the onset stress of precursor avalanches, to account for the Hookean strain along with the linear drift. In Fig. S6 (b), we subtract the linearly fitted strain from the overall unloading/reloading strain for the drift-corrected hysteresis behavior. The deformation left is plastic only.

Appendix E: Weighted fit and significance

We characterize the decay behavior of the precursor dissipation, U, versus number of cycles, n, using a fitting function $U_f(n)$[2],

$$U_f(n) = (U_0 - U_\infty)e^{-n/\tau}n^{-\delta} + U_\infty,$$

where we set the steady value $U_\infty = U_f(n \to \infty)$ to be zero for the steps with maximum loading stress below the critical stress. For the last step with maximum stress exceeding the critical stress, we verified that $\tau \sim 50$, so we estimate U_∞ to be the decayed dissipation at the end of the 100 cycles. δ is evaluated from a simple power law fitting to the approximate critical behavior at $\sigma_{\max} \sim \sigma_c$,

$$U_f'(n) = U_f(n;\ \tau \to \infty, U_\infty \to 0) = U_0 n^{-\delta}.$$

We use the 500 cycle training data at stress step $\sigma_{\max} = 1.08\ \sigma_c$ for the power-law fitting for δ, as shown in Figure S7. Over long cycles with the engineering maximum stress prescribed to be constant, the large plastic deformation in high-symmetry direction can cause a decrease in the true maximum stress applied to the sample due to volume conservation. As cycling at the stress level above the critical stress goes, the maximum stress eventually falls below the critical stress over large precursor strain – the precursor dissipation does not decay to finite steady-state value over long cycling tests.

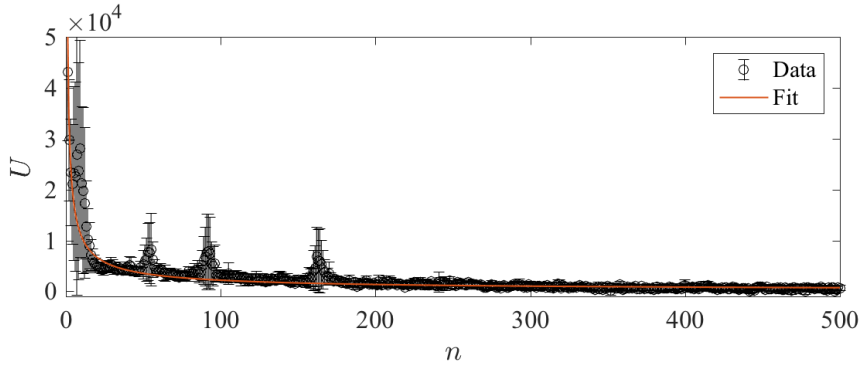

FIG. S7. **Power-law fitting to long-cycle training behavior.** The precursor dissipation vs. cycle behavior at the stress $\sigma_{\max} \sim \sigma_c$ is approximately critical and can be characterized by a simple

power-law decay for the fitting of the power-law exponent δ in the general model. The mean value spikes at n ~ 55, 92, 162 are occasional large precursor avalanches present in individual tests.

We apply the fitted mean power-law exponent $\delta = 0.68$ to the general model fitting for all stress steps. U_0 is the initial value of U_f. The fitting parameters, τ and U_0, as well as their confidence intervals were fitted using a nonlinear regression model featuring the Levenberg-Marquardt nonlinear least squares algorithm[3,4]. Each data point is weighted by the measurement error. The estimation error for the k-th parameter is taken as the 95% confidence interval, $2\sigma_k$.

Appendix F: Effect of stress rate on precursor dissipation

We apply fast unload-reload cycles with a symmetric loading rate of ~ 570 MPa/s in the training experiment to help reduce the effect of instrumental drift problem. However, the loading rate are too fast to be considered quasistatic. It is therefore reasonable to suspect that the precursor dissipations could have arisen from the fast loading rates. To address this issue, we performed small stress amplitude (~ 40 MPa) training tests on 3 μm diameter pillars using 3 different stress rates (40 MPa/s, 290 MPa/s, and 570 MPa/s), and calculated the corresponding precursor dissipation over number of cycles. No drift corrections are applied because of the small stress amplitude which leads to short linear segment for fitting. The results are shown in Fig. S8 in an increasing stress rate order; it is clear that for all three loading rates the system demonstrate a decay behavior of the precursor dissipation over number of cycles.

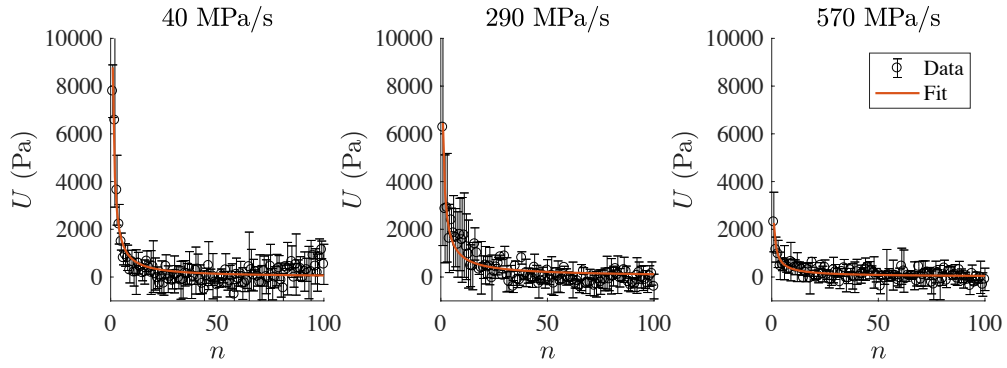

FIG. S8. **Precursor dissipation over number of cycles data and the decay behavior fit for training experiments with different loading/unloading stress rate** of 40 MPa/s, 290MPa/s, and 570 MPa/s.

The decay time constants for the three tests are estimated to be $6.8 \pm 1.8, 9.8 \pm 3.9$, and 7.2 ± 5.9. This ensures that the precursor avalanches and their self-organizing behavior

are not generated by fast loading. On the other hand, the initial precursor dissipation is larger in the slower loading experiments. The emergent stress rate dependency might relate to intrinsic time scales of the small-scale crystal, such as dislocation relaxation rate.

Appendix G: Precursor dissipation training for different Pillar sizes

In addition to 3 μm diameter pillars, we have also performed training tests on 0.5 μm and 1 μm diameter pillars. For 0.5 μm pillars, a total of twenty-six pillars were tested using six different maximum stresses ranging from 550 MPa to 800 MPa, with increments of 50 MPa. For 1μm pillars, we tested seven pillars using five different maximum stresses ranging from 300 MPa to 600 MPa with increments of 75 MPa.

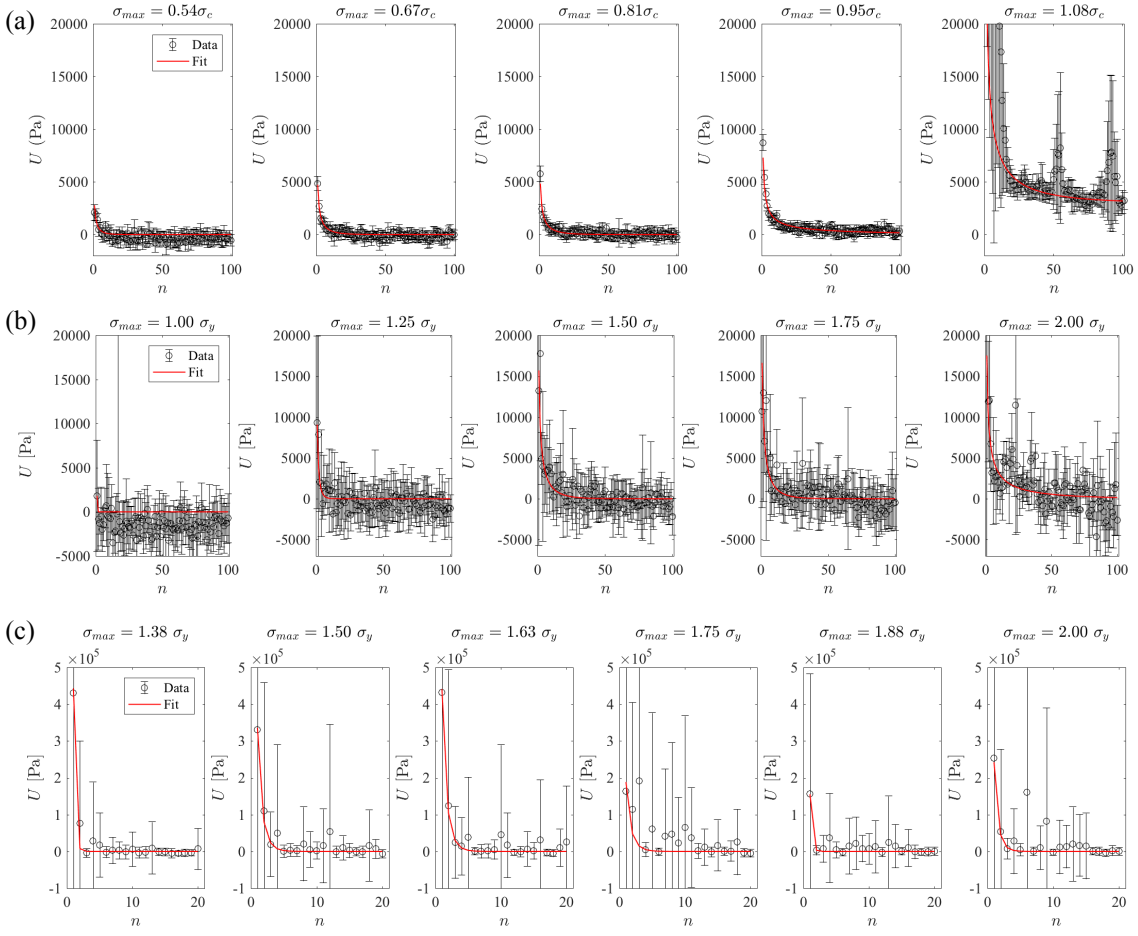

FIG. S9. **Precursor area vs. number of cycle data for (a) 3 μm, (b) 1 μm, and (c) 0.5 μm diameter pillars.** For all sizes and in all steps (with $\sigma_{max} < \sigma_c$), the precursor dissipation can be trained away after a certain number of cycles. The magnitudes of precursor dissipation are in general larger in smaller size pillars. The initial precursor dissipation for (a) 3 μm, and (b) 1 μm pillars, grows as the maximum stress grows; the decay time increases with stress. (c) There is no conclusive trend on the decay time constant for 500 nm pillars.

For both training tests, we unload to a constant minimum stress of 100 MPa to maintain contact between the actuation punch and the sample. Following the same analysis procedures described for 3 μm diameter pillars, the cyclic precursor dissipations were examined for both sizes of pillars. The results are shown in Fig. S9 above. It is worth noting that the training tests for 0.5 μm diameter pillars have too small loading/unloading amplitudes for drift correction.

For all sizes of pillars, the precursor dissipation can be trained away after a certain number of cycles. From the available data, we can hardly distinguish the training behaviors at different maximum stresses. For 1 μm pillars, the initial precursor dissipation grows as the maximum stress grows; the behavior of the decay time also increases with stress (See Fig 3(b) in the main text).

Appendix H: Power-law exponent sweep

The power-law exponent δ in the fitting model is obtained from an approximation for the critical point behavior – we fit for the exponent from a pure power-law fitting for the cyclic precursor dissipation data at stress step close to the critical stress as. It is necessary to investigate the error tolerance for the fitted δ: the power-law divergent behavior of the fitted time scale τ should not be sensitive to the changes of the prescribed power law component δ in a range. We evaluate this range by investigating fitted τ vs. σ_{max} for different values of δ.

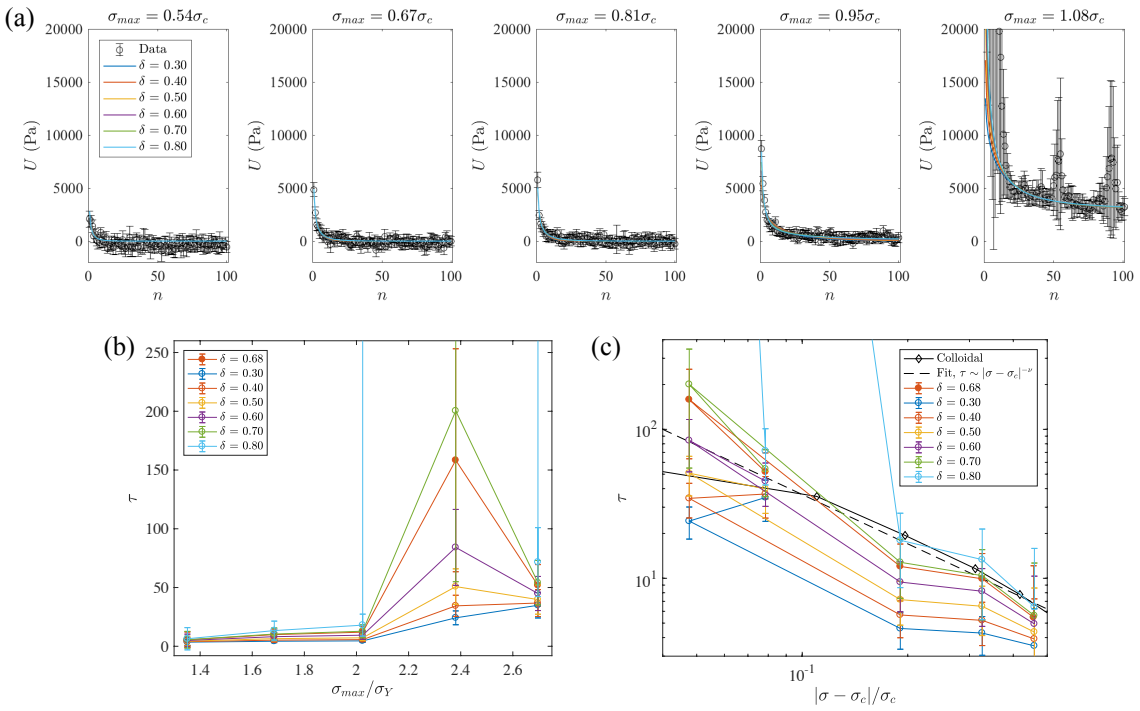

FIG. S10. **Fitting for decay time constant τ for 3 μm diameter pillars with different power-law exponent δ values.** Different δ-value fits are represented by different colors. (a) Fittings to U vs. n at increasing maximum stress, (b) fitted τ vs. σ_{max}, and (c) a scaling analysis of τ vs. σ_{max} for 3 μm diameter pillars with different δ values.

The fittings to the 3 μm diameter pillar cyclic precursor dissipation data using different values of δ, sweeping the range 0.1 ~ 0.7 in a 0.1 interval, are shown in Figure S10 (a) in different colors. Fig. S10 (b) show the fitted τ vs. σ_{max} with the same δ sweep. The scaling analysis of τ shown in Fig. S10 (c) demonstrates that the divergent behavior of the training time constant does not change much when δ is in the range 0.4 ~ 0.5.

1. Ni, X., Papanikolaou, S., Vajente, G., Adhikari, R. X. & Greer, J. R. Probing Microplasticity in Small-Scale FCC Crystals via Dynamic Mechanical Analysis. *Phys. Rev. Lett.* **118,** (2017).
2. Corté, L., Chaikin, P. M., Gollub, J. P. & Pine, D. J. Random organization in periodically driven systems. *Nat. Phys.* **4,** 420–424 (2008).
3. Marquardt, D. W. An Algorithm for Least-Squares Estimation of Nonlinear Parameters. *J. Soc. Ind. Appl. Math.* **11,** 431–441 (1963).
4. Press, W., Flannery, B., Teukolsky, S. & Vetterling, W. *Numerical Recipes*. *Cambridge University Press. Cambridge, NY* (1986).